

Structural, elastic, bonding, optoelectronic, and some thermo-physical properties of transition metal dichalcogenides ZrX_2 ($X = S, Se, Te$): Insights from ab-initio calculations

*Md. Mahamudujjaman, Md. Asif Afzal, R. S. Islam, S. H. Naqib**
Department of Physics, University of Rajshahi, Rajshahi 6205, Bangladesh
**Corresponding Author; Email: salehnaqib@yahoo.com*

Abstract

Transition metal dichalcogenides (TMDCs) belong to technologically important compounds. We have explored the structural, elastic, bonding, optoelectronic and some thermo-physical properties of ZrX_2 ($X = S, Se, Te$) TMDCs in details via ab-initio technique in this study. Elastic anisotropy indices, atomic bonding character, optoelectronic properties and thermo-physical parameters including melting temperature and minimum phonon thermal conductivity are investigated for the first time. All the TMDCs under investigation possess significant elastic anisotropy and layered structural features. ZrX_2 ($X = S, Se, Te$) compounds are fairly machinable, and ZrS_2 and $ZrSe_2$ are moderately hard. $ZrTe_2$, on the other hand, is significantly softer. Both covalent and ionic bondings contribute in the crystals. Electronic band structure calculations display semiconducting behavior for ZrS_2 and $ZrSe_2$ and metallic behavior for $ZrTe_2$. Energy dependent optoelectronic parameters exhibit good correspondence with the underlying electronic energy density of states features. ZrX_2 ($X = S, Se, Te$) compounds absorb ultraviolet radiation effectively. The reflectivity spectrum, $R(\omega)$, remains over 50% in the energy range from 0 eV to ~ 20 eV for $ZrTe_2$. Therefore, this TMDC has wide band and nonselective high reflectivity and can be used as an efficient reflector to reduce solar heating. Debye temperature, melting point and minimum phonon thermal conductivity of the compounds under study are low and show excellent correspondence with each other and also with the elastic and bonding characteristics.

Keywords: Transition metal dichalcogenides; Elastic properties; Electronic band structure; Bonding character; Optoelectronic properties

1. Introduction

Transition metal dichalcogenides (TMDCs) [1–3] are crystalline solids with layered structure. The TMDCs have attracted notable attention of researchers primarily due to their potential electrochemical applications. They display widespread electronic properties such as metallic [4–6], semi-metallic [7–10], semiconducting [11–14], charge density waves [15,16], magnetic order [17–19] and superconductivity [20–22] attained mainly by electronic band structure engineering [23–25]. Binary TMDCs are materials that have unique mechanical, electric and optical

properties, and have become potential rivals in the field of spintronics [26–30] as well as in optoelectronics [31–35]. I. Kar et al. [36] showed that electronic phase transition can occur from semiconducting to topological semi-metal in going from ZrSe_2 to ZrTe_2 by changing metal-chalcogen bond lengths. Binary TMDC topological semi-metals with nontrivial electronic structure exhibiting low-dissipation transport at room temperature can reduce power consumption and heating of conventional electronic equipments [37]. Furthermore, topological insulators and semi-metals have potential applications in quantum computation, novel optoelectronic and thermoelectric power harvesting devices.

One of the major advantages of binary TMDCs is tunable bandgap associated to a strong photoluminescence and large exciton binding energy that make them potential candidates for a variety of optoelectronic devices along with solar cells, photo detectors, light emitting diodes (LEDs), photo transistors, field effect transistors (FETs), and logic transistors [23,38–41]. As the TMDCs have layered structures and these layers are interconnected by weak interactions, foreign atoms or molecules can be inserted into the gap (the so called van der Waals gap) forming various intercalated compounds. Intercalation is an effective and efficient means for electronic band structure manipulation. Because of layered structures they can also be applied as dry lubricants [42,43].

In this study, three TMDC materials, ZrX_2 ($X = \text{S, Se, Te}$) are explored by the Kohn-Sham density functional theory (KS-DFT). There are some previous theoretical works on our chosen materials [36,44–46]. In those articles, structural, elastic, electronic and optical dielectric properties are studied. But still there are notable shortages of information on these materials. These lacks of information limit the feasibility of potential applications. Various thermo-physical properties, chemical bonding properties and charge density distribution of these materials have not been studied yet. Besides, a complete theoretical understanding of the optical properties is still lacking. So in this work, we have performed a broader investigation to bridge the existing knowledge gap. We have studied structural, elastic, bonding, charge density distribution, electronic, optical and thermo-physical properties of ZrX_2 ($X = \text{S, Se, Te}$). ZrS_2 and ZrSe_2 are semiconductors, and the band gaps fall in the visible-infrared region, that's why they could be potential candidates in photovoltaic device applications [47]. ZrTe_2 , on the other hand, is metallic. The elastic, thermal and optical parameters exhibit a number of features pertinent to potential applications.

The rest of the paper is constructed in the following manner: In Section 2, we have discussed the computational methodology in detail. In Section 3, we have described the crystal structure, presented the computational results and analyzed those. Finally, the important findings of our calculations are discussed and summarized in Section 4.

2. Computational methodology

Density functional theory (DFT) is the most widely employed formalism for ab-initio calculations in crystalline solids where the ground state of crystalline system is found by solving the Kohn-Sham equation [48] with periodic boundary conditions (involving Bloch states). Here DFT based Cambridge Serial Total Energy Package (CASTEP) code [49] has been used to explore various physical properties of the titled compounds. This code implements the total energy plane-wave pseudopotential method. In this study, we have used both local density approximation (LDA) and generalized gradient approximation (GGA) exchange-correlation functionals. It is well known that, LDA has a tendency of underestimating the lattice constants. On the other hand, GGA tends to overestimate the lattice constants. We have used both to check the suitability regarding the compounds of interest. In comparison with experimental lattice constants, GGA provides better results of ground state structural parameters for ZrX_2 ($X = S, Se, Te$). The most popular GGA functional, known as Perdew-Burke-Ernzerhof (PBE) scheme [50], tend to overestimate equilibrium volume more whereas it's modified version known as the PBEsol [51] accounts for better equilibrium volume. In PBEsol the two parameters of PBE are changed in order to satisfy the constraints that are more congenial for solids, except that, both functionals have the same analytical form. Therefore, the results reported herein are obtained using the GGA-PBEsol scheme. The electron-ion interaction is modeled by the Vanderbilt-type ultra-soft pseudopotential. This pseudopotential saves the computational time significantly without affecting the accuracy of the calculations to a large extent [52].

The valence electron configurations of Zr, S, Se, and Te have been taken as $[4d^25s^2]$, $[3s^23p^4]$, $[4s^24p^6]$ and $[5s^25p^4]$, respectively. Periodic boundary conditions are used to determine the total energies of each cell. In this paper, $18 \times 18 \times 12$ k-points mesh is used based on Monkhorst-Pack scheme [53] for sampling the Brillouin zones of ZrX_2 ($X = S, Se, Te$) with a cut-off energy of 500 eV. On the other hand, to obtain a smooth Fermi surface of $ZrTe_2$, $32 \times 32 \times 18$ k-points mesh has been used. The crystal geometry optimization is achieved through minimizing the total energy applying the Broyden-Fletcher-Goldferb-Shanno (BFGS) minimization technique [54]. The structure is relaxed up to a convergence threshold of 5×10^{-6} eV-atom⁻¹ for energy, 0.01 eV Å⁻¹ for the maximum force, 0.02 GPa for maximum stress and 5×10^{-4} Å for maximum displacement. The independent single crystal elastic constants C_{ij} , bulk modulus B, shear modulus G are calculated from the 'stress-strain' method contained within the CASTEP code. The electronic band structure, total density of states (TDOS) and partial density of states (PDOS) are obtained from the optimized geometry of ZrX_2 ($X = S, Se, Te$). The frequency-dependent optical properties are extracted from the estimated complex dielectric function, $\epsilon(\omega) = \epsilon_1(\omega) + i\epsilon_2(\omega)$, which describes the frequency/energy dependent interactions of photons with electrons in solids. Using the Kramers-Kronig relationships, the real part $\epsilon_1(\omega)$ of dielectric function $\epsilon(\omega)$ has been obtained from the imaginary part $\epsilon_2(\omega)$. The imaginary part, $\epsilon_2(\omega)$, is calculated within the momentum representation of matrix elements of transition between occupied and unoccupied electronic states by employing the CASTEP supported formula expressed as:

$$\epsilon_2(\omega) = \frac{2e^2\pi}{\Omega\epsilon_0} \sum_{k,v,c} |\langle \psi_k^c | \hat{u} \cdot \vec{r} | \psi_k^v \rangle|^2 \delta(E_k^c - E_k^v - E) \quad (1)$$

where, Ω is the volume of the unit cell, ω is angular frequency of the incident electromagnetic wave (photon), e is the electronic charge, ψ_k^c and ψ_k^v are the conduction and valence band wave functions at a given wave-vector k , respectively. The conservation of energy and momentum during the optical transition is implemented by the delta function. When the dielectric function $\epsilon(\omega)$ is known, all the optical parameters such as refractive index, optical conductivity, reflectivity, absorption coefficient, and energy loss function can be computed from it. The Debye temperature and other thermo-physical parameters are calculated from elastic constants and elastic moduli of ZrX_2 ($X = S, Se, Te$) via the average sound velocity in the compounds of interest.

Many previous studies showed that, spin orbit coupling (SOC) has minimal effect on bulk physical properties, such as the optimized crystal structure, elastic constants, mechanical anisotropy, chemical bonding, thermo-physical behavior, bulk optical properties, etc [55–57]. Since our attention is on the bulk physical properties of the chosen materials which do not contain significant topological electronic features, we did not include SOC in the calculations to follow.

3. Results and analysis

I. Structural properties

The ZrX_2 ($X = S, Se, Te$) compounds are isostructural and crystallize in $1T-CdI_2$ type structure with space group $P-3m1$ (no.164) in which octahedrally-coordinated X-Zr-X type sandwich layers are stacked with a periodicity of one layer possessing globally trigonal symmetry [58]. Due to van der Waals interaction, the interlayer bonding is weak while the intralayer Zr-X ionic bonding is strong [45]. The schematic crystal structure of ZrX_2 ($X = S, Se, Te$) is shown below in Fig. 1.

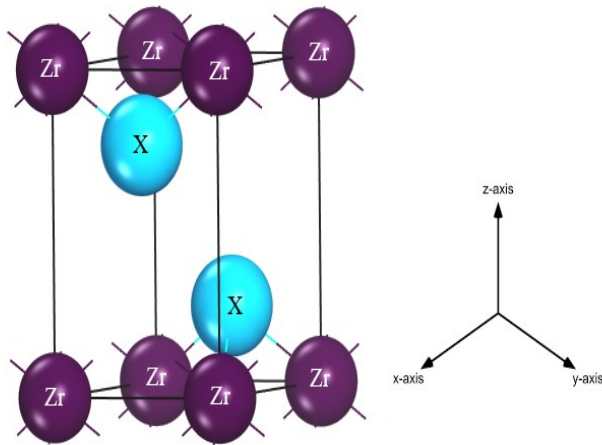


Figure 1. Schematic crystal structure of ZrX_2 ($X = S, Se, Te$) compounds.

Each unit cell of ZrX_2 ($X = S, Se, Te$) contains one formula unit and 10 atoms (8 Zr and 2 X) in total. Zr occupies 1c site (0 0 0) and X occupies 2d site ($1/3 \ 2/3 \ \pm z$). The only free structural parameter z , approximately equals to $1/4$ in equilibrium. So in this study, we use $1/4$ as the value of z . The optimized lattice parameters along with available theoretical and experimental lattice parameters are listed in the Table 1. The calculated lattice parameters of titled materials show good agreement with theoretical and experimental results. As mentioned earlier, application of LDA and GGA-PBE increases the deviations among theoretical and experimental structural parameters.

In Table 1 one observes that the equilibrium volumes obtained using GGA-PBEsol are slightly lower than that of experimental values which may appear somewhat unexpected. But it is worth noting that, the experimental structural parameters are determined at room temperature while the *ab-initio* calculations are performed assuming absolute zero temperature.

Table 1. Optimized lattice parameters ($a = b$ in Å, c in Å, equilibrium volume V_0 in Å³) of ZrX_2 ($X = S, Se, Te$) as compared to available theoretical and experimental data.

Compound	a	c	c/a	V_0	Ref.
ZrS ₂	3.628	5.879	1.620	67.049	This
	3.661	5.815	1.588	67.496	[59] ^{Expt.}
	3.629	5.884	1.621	67.108	[46] ^{Theo.}
ZrSe ₂	3.713	6.060	1.632	72.378	This
	3.766	6.150	1.633	75.538	[36] ^{Expt.}
	3.732	6.134	1.643	73.987	[46] ^{Theo.}
ZrTe ₂	3.884	6.641	1.710	86.751	This
	3.945	6.624	1.679	89.278	[36] ^{Expt.}
	3.909	6.749	1.726	89.310	[36] ^{Theo.}

II. Elastic properties

In order to ensure structural/mechanical stability, it is very important to calculate elastic constants. Using single crystal elastic constants, various elastic properties can be determined. ZrX_2 ($X = S, Se, Te$) has trigonal crystal structure. This structure has six independent elastic constants (C_{ij}). These elastic constants are: C_{11} , C_{33} , C_{44} , C_{12} , C_{13} and C_{14} . The calculated elastic constants of the titled compounds are listed in Table 2. According to Born-Huang conditions, a trigonal crystal system needs to satisfy the following criteria for mechanical stability [60]:

$$C_{11} - C_{12} > 0;$$

$$(C_{11} - C_{12})C_{44} - 2C_{14}^2 > 0;$$

$$(C_{11} + C_{12})C_{33} - 2C_{13}^2 > 0 \quad (2)$$

All the elastic constants of ZrX_2 ($X = S, Se, Te$) satisfy the mechanical stability criteria. This suggests that these TMDCs are mechanically stable. It is interesting to note that, small negative values of C_{14} have no bearing on the mechanical stability of ZrS_2 and $ZrSe_2$. This may rather indicate that there are small internal strains in the optimized geometries of these crystals.

Table 2. Single crystal elastic constants, C_{ij} , of ZrX_2 ($X = S, Se, Te$) (all in GPa)

Compound	C_{11}	C_{33}	C_{44}	C_{12}	C_{13}	C_{14}	Ref.
ZrS_2	130.67	22.64	6.86	23.07	0.83	-3.08	This
	131.47	29.93	52.92	25.63	4.25	-	[45]
$ZrSe_2$	116.91	30.31	18.64	24.03	6.37	-6.88	This
	104.62	29.96	41.66	21.31	5.01	-	[45]
$ZrTe_2$	67.65	32.30	6.94	12.95	8.07	1.07	This
	69.00	26.00	31.00	-	-	-	[44]

Among the six independent single crystal elastic constants, C_{11} and C_{33} determine the ability of the crystal to resist the mechanical stress applied along the crystallographic a- (b-) and c-directions, respectively. From Table 2 we can see that, for all the compounds C_{11} is greater than C_{33} . This suggests that the structure is more compressible in the c-direction than in a-direction. This is indicative of the layered nature of the compounds under study. This infers that the chemical bonding in the ab-plane is stronger than that in the out-of-plane direction. The resistance to shear deformation with respect to a tangential stress applied across the (100) plane in the [010] direction is quantified by elastic constant, C_{44} . Here $C_{44} < C_{11}$ and C_{33} , which suggests that the compounds are more easily deformed by a shear in comparison to a unidirectional compression along any of the three crystallographic directions. The other elastic constants C_{12} , C_{13} , and C_{14} are called off-diagonal shear components, which are related with compound's resistance due to various shape distortions.

Different types of elastic moduli, indicators and Poisson's ratio can be obtained from the single crystal elastic constants, C_{ij} . As single crystal samples are hard to synthesize and in many cases not practically applicable on large scale, information regarding elastic constants for polycrystalline aggregates are important for applications point of view. Table 3 exhibits the polycrystalline bulk modulus (B), Shear modulus (G), Pugh's ratio (B/G), Young's modulus (Y) and Poisson's ratio (η). In his treatment of elastic moduli for polycrystalline solids, Voigt [61] assumed that strain is uniform throughout the aggregate and derived effective isotropic stiffnesses in terms of space averages of the single crystal elastic stiffnesses over all possible orientations. This approximation gives us the upper limit of the polycrystalline elastic moduli. Reuss [62], on the other hand, assumed uniform stress throughout the polycrystal and derived effective isotropic elastic compliances in terms of single-crystal elastic compliances averaged over all orientations resulting in the lower limit of the polycrystalline elastic moduli. The real

value lies between Voigt and Reuss bounds. Hill [63] later proposed the arithmetic average of the two limits, which closely represents the practical situation.

The bulk modulus describes the material's response to the volume changing hydrostatic pressure and the shear modulus measures the material's resistance against shape deforming shear stress. From Table 3, it is evident that B is greater than G for all the compounds. Therefore, the mechanical stabilities of ZrX_2 ($X = S, Se, Te$) are expected to be controlled by shearing strain.

Table 3. Elastic moduli (all in GPa), Pugh's ratio, and Poisson's ratio of ZrX_2 ($X = S, Se, Te$) compounds.

Compound	B_V	B_R	B_H	G_V	G_R	G_H	B/G	Y	η	Ref.
ZrS_2	37.052	17.782	27.417	30.786	12.459	21.622	1.267	51.365	0.187	This
	40.120	23.330	31.730	31.490	16.210	23.850	1.330	57.22	0.200	[45]
$ZrSe_2$	37.523	23.805	30.664	31.901	23.498	27.699	1.107	63.867	0.152	This
	33.540	22.450	27.990	26.560	17.470	22.020	1.270	52.33	0.190	[45]
$ZrTe_2$	25.090	21.905	23.497	17.478	11.781	14.629	1.606	36.346	0.242	This
	-	-	-	-	-	-	-	-	-	-

The ratio B/G, called the Pugh's ratio is an indicator of the ductile or brittle nature of a compound. If the value of Pugh's ratio is greater than 1.75, the material is predicted to be ductile in nature; otherwise the material should exhibit brittleness [64]. Thus all the materials in this work are expected to show brittle behavior. Poisson's ratio (η) is a measure of materials deformation (expansion or contraction) along the perpendicular direction of loading. It also gives a measure of the stability of solids against shear. If $\eta = 0.5$, no volume change occur during elastic deformation. For ZrX_2 ($X = S, Se, Te$) compounds, η is much lower than 0.5 which means a large volume change is associated during elastic deformation. Poisson's ratio is an important parameter that determines various mechanical properties of crystalline solids. It can predict the ductility or brittleness of materials with the critical value of 0.26. If η is less (greater) than 0.26, the material is brittle (ductile). Thus, this judgment criteria tells us that ZrX_2 ($X = S, Se, Te$) compounds are brittle. This is consistent with the result obtained from the Pugh's ratio. The value of η also can predict the nature of interatomic forces in solids [65,66]. If η remains between 0.25 and 0.50, central force interaction will dominate. Otherwise non-central force will dominate. Thus, in ZrX_2 ($X = S, Se, Te$) non-central force should dominate the atomic bonding. In completely ionic bonded solids, the value of η is approximately 0.33, while in purely covalent bonded crystal, it is around 0.10. This implies that, in ZrS_2 and $ZrSe_2$ covalent bondings should be dominant and in $ZrTe_2$ ionic bonding should be dominant. The overall bonding characters of the TMDCs under consideration should exhibit mixed character with different proportions of

covalent and ionic contributions. Besides, Poisson's ratio signifies the level of plasticity of a solid against shear. Larger the Poisson's ratio better is the plasticity.

A number of useful mechanical performance indicators, namely the machinability index (μ^M), Kleinman parameter (ζ) and Vickers hardness (H_V) are calculated using the following widely employed equations [67,68] and are listed in Table 4.

$$\mu^M = \frac{B}{C_{44}} \quad (3)$$

$$\zeta = \frac{C_{11} + 8C_{12}}{7C_{11} + 2C_{12}} \quad (4)$$

$$H_V = \frac{(1 - 2\eta)Y}{6(1 + \eta)} \quad (5)$$

The machinability index is also a measure of dry lubricating nature of a material. A high value of μ^M indicates excellent lubricating properties, i.e., lower friction. The value of μ^M in ZrX_2 ($X = S, Se, Te$) implies a good level of machinability which compares favorably to many technologically important MAX phase nanolaminates [69–73]. The machinability indices of ZrS_2 and $ZrTe_2$ are particularly high. Generally, the value of Kleinman parameter lies between 0 and 1. According to Kleinman, the lower limit of ζ represents significant contribution of bond stretching or contracting to resist external stress whereas the upper limit corresponds to significant contribution of bond bending to resist external load. From Table 4, it is evident that, mechanical strength in ZrX_2 ($X = S, Se, Te$) is mainly derived from the bond stretching/contracting contribution. The hardness of a solid is essential to understand elastic and plastic properties.

The bulk modulus along a-, b- and c-axis (known as directional bulk modulus) and isotropic bulk modulus (B_{relax}) are defined as follows [68] and are also enlisted in Table 4.

$$B_a = a \frac{dP}{da} = \frac{\Lambda}{1 + \alpha + \beta} \quad (6)$$

$$B_b = b \frac{dP}{db} = \frac{B_a}{\alpha} \quad (7)$$

$$B_c = c \frac{dP}{dc} = \frac{B_a}{\beta} \quad (8)$$

$$B_{relax} = \frac{\Lambda}{(1 + \alpha + \beta)^2} \quad (9)$$

where, $\Lambda = C_{11} + 2C_{12}\alpha + C_{22}\alpha^2 + 2C_{13}\beta + C_{33}\beta^2 + 2C_{23}\alpha\beta$

and

$$\alpha = \frac{\{(C_{11} - C_{12})(C_{33} - C_{13})\} - \{(C_{23} - C_{13})(C_{11} - C_{13})\}}{\{(C_{33} - C_{13})(C_{22} - C_{12})\} - \{(C_{13} - C_{23})(C_{12} - C_{23})\}}$$

$$\beta = \frac{\{(C_{22} - C_{12})(C_{11} - C_{13})\} - \{(C_{11} - C_{12})(C_{23} - C_{12})\}}{\{(C_{22} - C_{12})(C_{33} - C_{13})\} - \{(C_{12} - C_{23})(C_{13} - C_{23})\}}$$

The calculated B_{relax} using Eqn. 9 gives the same value as the Reuss approximation does. α and β are the relative change of the b- and c- axis as a function of the deformation of the a axis. The small value of B_c compared to B_a and B_b indicates that ZrX_2 ($X = S, Se, Te$) are more compressible when stress is applied along c-direction than along a- or b-direction.

Table 4. The machinability index (μ^M), Kleinman parameter (ζ), Vickers hardness (H_v in GPa), bulk modulus (B_{relax} in GPa), bulk modulus along a-, b- and c-axis (B_a, B_b, B_c in GPa), α and β of ZrX_2 ($X = S, Se, Te$) compounds.

Compound	μ^M	ζ	H_v	B_{relax}	B_a	B_b	B_c	α	β	Ref.
ZrS ₂	3.996	0.328	6.582	17.782	102.66	102.66	14.723	1	6.972	This
ZrSe ₂	1.644	0.356	6.411	23.805	175.091	175.091	32.695	1	5.355	This
ZrTe ₂	3.385	0.342	2.513	21.905	102.083	102.083	38.375	1	2.66	This

It is instructive to notice that ZrS₂ and ZrSe₂ are reasonably hard compounds while ZrTe₂ is significantly softer. All the results displayed in Table 4 are novel and there is no existing data to be compared.

It is worth stating that elastic anisotropy has influence on development of plastic deformation in crystals, formation and propagation of microscale cracks in ceramics, plastic relaxation in the thin films etc. Therefore, it is quite important to evaluate the elastic anisotropy factors for solids to predict their behavior under different conditions of external stresses [73–75]. The elastic/mechanical anisotropy indices of ZrX_2 ($X = S, Se, Te$) are investigated in this section. We have calculated Zener anisotropy factor (A), shear anisotropy factors (A_1, A_2, A_3), percentage anisotropy in compressibility (A_B) and shear (A_G), universal anisotropy factor (A^U, d_E), Equivalent Zener anisotropy factor (A^{eq}) and disclosed those in Table 5. The following widely used relations are used to calculate anisotropy factors [76–78]:

$$A = \frac{2C_{44}}{C_{11} - C_{12}} \quad (10)$$

$$A_1 = \frac{4C_{44}}{C_{11} + C_{33} - 2C_{13}} \quad (11)$$

$$A_2 = \frac{4C_{55}}{C_{22} + C_{33} - 2C_{23}} \quad (12)$$

$$A_3 = \frac{4C_{66}}{C_{11} + C_{22} - 2C_{12}} \quad (13)$$

$$A_B = \frac{B_V - B_R}{B_V + B_R} \quad (14)$$

$$A_G = \frac{G_V - G_R}{G_V + G_R} \quad (15)$$

$$A^U = \frac{B_V}{B_R} + 5\frac{G_V}{G_R} - 6 \geq 0 \quad (16)$$

$$d_E = \sqrt{A^U + 6} \quad (17)$$

$$A^{eq} = \left(1 + \frac{5}{12}A^U\right) + \sqrt{\left(1 + \frac{5}{12}A^U\right)^2 - 1} \quad (18)$$

The calculated values of A , A_1 and A_2 are significantly different from 1. These anisotropy factors imply that ZrX_2 ($X = S, Se, Te$) are strongly anisotropic with respect to shearing stress along different crystal planes. But there is an exception, the shear anisotropy factor $A_3 = 1$ for ZrX_2 ($X = S, Se, Te$), which means that for $\{001\}$ shear planes between $\langle 110 \rangle$ and $\langle 010 \rangle$ directions, the compounds are isotropic in nature. For A_B and A_G , zero value represents elastic isotropy and a value of 1 corresponds to highest anisotropy. Therefore, from Table 5, it is evident that the compounds under study are anisotropic in compressibility and shear. An anisotropy factor A^U , known as the universal anisotropy factor because of its applicability to all kinds of crystal symmetries was defined by Ranganathan and Ostoja-Starzewski [79]. For elastically isotropic crystals $A^U = 0$, while any other positive value indicates anisotropy. The calculated values of A^U suggests that, ZrX_2 ($X = S, Se, Te$) compounds possess large amount of anisotropy in elastic properties. For A^{eq} , a value of 1 represents isotropy, while any other value indicates anisotropy. Thus, the values of A^{eq} for ZrX_2 ($X = S, Se, Te$) indicate that the compounds under investigations are highly anisotropic. All the anisotropy indices reflect of structural anisotropy which originates from the anisotropy in the bonding strengths in different directions in the unit cell of the crystal.

The universal log-Euclidean index is defined by the following equation [77]:

$$A^L = \sqrt{\left[\ln\left(\frac{B_V}{B_R}\right)\right]^2 + 5\left[\ln\left(\frac{C_{44}^V}{C_{44}^R}\right)\right]^2} \quad (19)$$

where,

$$C_{44}^R = \frac{5}{3} \frac{C_{44}(C_{11} - C_{12})}{3(C_{11} - C_{12}) + 4C_{44}} \text{ is the Reuss value of } C_{44}$$

$$C_{44}^V = C_{44}^R + \frac{3}{5} \frac{(C_{11} - C_{12} - 2C_{44})^2}{3(C_{11} - C_{12}) + 4C_{44}} \text{ is the Voigt value of } C_{44}$$

According to Kube and Jong [80], the value of A^L lies in the range $0 \leq A^L \leq 10.26$ for inorganic crystalline compounds and 90% of these compounds have $A^L < 1$. For perfect isotropy, $A^L = 0$. Based on the value of A^L , it is difficult to ascertain whether a material is layered/lamellar or not. But, the majority (78%) of these inorganic crystalline compounds with high A^L value exhibit layered/lamellar structure [80]. Based on the above discussion, we predict that the compounds under investigation are highly anisotropic and layered in nature. The compound ZrS_2 is expected to exhibit very high level of layered feature in particular.

Table 5. Elastic anisotropy indices of ZrX_2 ($X = S, Se, Te$) compounds.

Compound	A	A_1	A_2	A_3	A_B	A_G	A^U	d_E	A^{eq}	A^L	A_{B_a}	A_{B_c}	Ref.
ZrS_2	0.127	0.18	0.18	1	0.351	0.423	8.438	3.799	8.92	3.763	1	0.143	This
$ZrSe_2$	0.401	0.554	0.554	1	0.223	0.151	2.364	2.892	3.699	1.199	1	0.186	This
$ZrTe_2$	0.253	0.331	0.331	1	0.067	0.194	2.563	2.926	3.878	2.123	1	0.375	This

The anisotropies of the bulk modulus along a- and c-axis are defined as [68]:

$$A_{B_a} = \frac{B_a}{B_b} = \alpha \quad (20)$$

$$A_{B_c} = \frac{B_c}{B_b} = \beta \quad (21)$$

The calculated values of A_{B_a} and A_{B_c} are also enlisted in Table 5 and the values represent that the bulk modulus for ZrX_2 ($X = S, Se, Te$) along a-axis is isotropic and along c-axis is anisotropic.

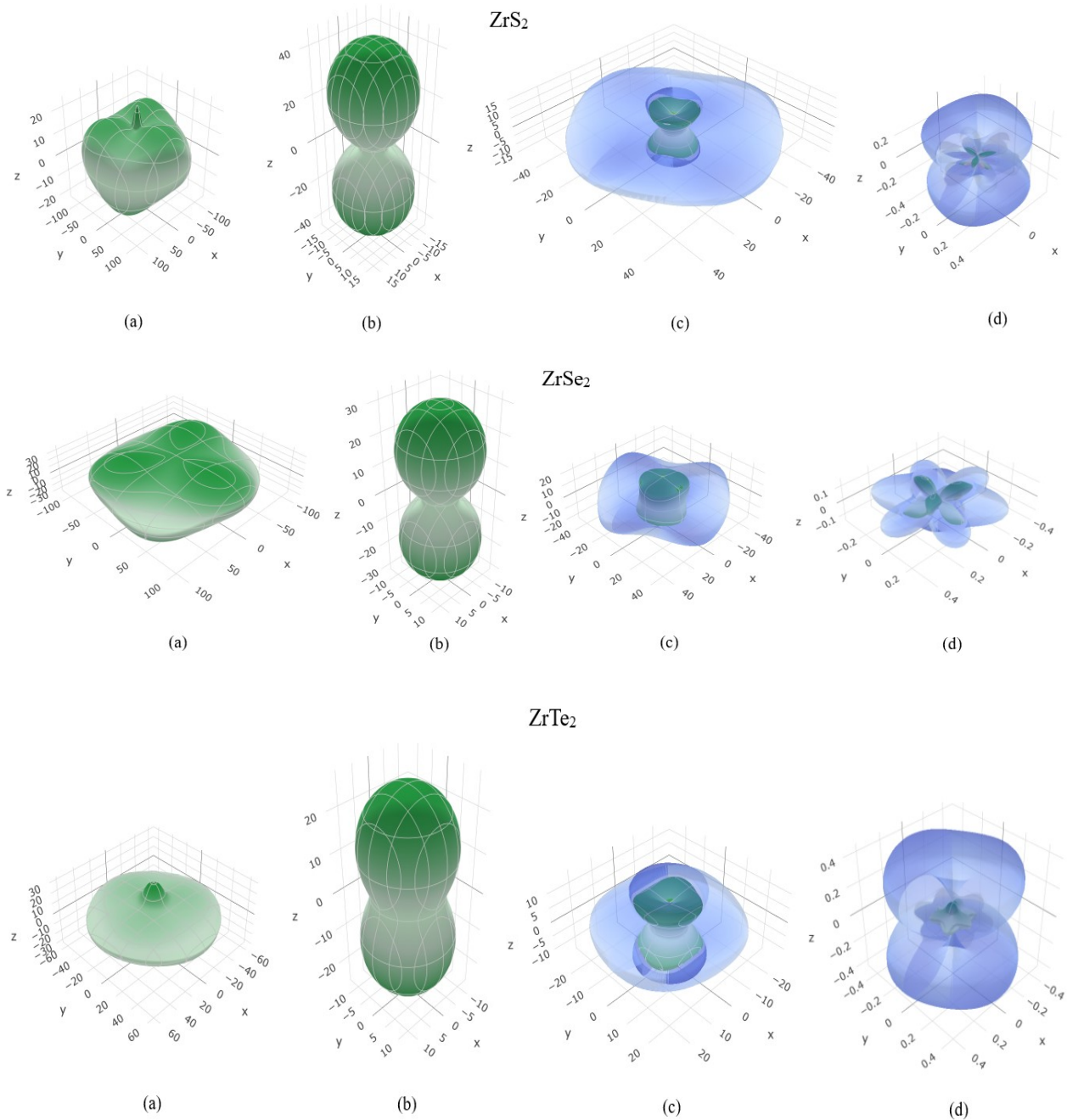


Figure 2. 3D directional dependences of (a) Young modulus (b) shear modulus (c) linear compressibility and (d) Poisson's ratio for ZrX_2 ($X = S, Se, Te$) compounds.

For isotropic solids, three dimensional (3D) direction dependent Young modulus, shear modulus, linear compressibility and Poisson's ratio should exhibit spherical shapes, while any deviation from spherical shape would indicate anisotropy. We have shown ELATE [81] generated 3D plots of directional dependence of Young modulus, shear modulus, linear compressibility and Poisson's ratio for ZrX_2 ($X = S, Se, Te$) compounds in Fig. 2 above.

III. Electronic band structure and density of states

(a) Electronic band structure

Electronic band structures for optimized crystal structure of ZrX_2 ($X = S, Se, Te$) along several high symmetry directions in the first Brillouin zone (BZ) are depicted in Fig. 3. The band structures of ZrS_2 and $ZrSe_2$ show that they have indirect minimal band gaps between valence band maxima at $\Gamma(k = (0,0,0))$ and conduction band minima at $L(k = (1/2,0,1/2))$. The direct and indirect band gap values of ZrS_2 and $ZrSe_2$ along with available experimental and theoretical values are given in Table 6.

Table 6. Calculated band gaps in eV of ZrS_2 and $ZrSe_2$ with available theoretical and experimental values.

Compounds	Band gap (E_g) type	Theoretical E_g [Ref.]	Experimental E_g [Ref.]
ZrS_2	Indirect	0.74 [This]	1.70[82]
		0.79 [46]	
	Direct	1.50 [This]	2.10[82]
		1.45 [46]	
$ZrSe_2$	Indirect	0.14 [This]	1.18 [82]
		0.21 [46]	
	Direct	1.04 [This]	1.61 [82]
		0.89 [46]	

It is well known that, in DFT use of GGA and LDA type exchange-correlations functionals underestimate the band gaps of semiconductors and insulators [82]. We have displayed the GGA results in Table 3 since it optimized the crystal structures most effectively. Though, indirect band gaps deviate from the other theoretical and available experimental values, direct band gaps show better agreement with theoretical [46] and experimental results [82]. The band structure diagram of $ZrTe_2$ shows that a number of bands (red and green curves) cross the Fermi level (E_F), which is indicated by a horizontal line placed at 0 eV. Therefore, $ZrTe_2$ is a metal. Highly dispersive nature of the bands crossing the Fermi level near Γ -point for $ZrTe_2$ is indicative of high mobility of the charge carriers in this compound. It is interesting to note that the band crossing near the Γ -point displays hole-like feature while the crossings near the A- and L-point of the BZ exhibit electron-like dispersions. Overall, for all three compounds under investigation, the curves along Γ -A, H-K directions are less dispersive, which indicates high effective mass of charge carriers and consequently low mobility in these directions. On the other hand, the band curves along A-H and K- Γ directions show high dispersion, which indicates low effective mass and high mobility of electrons. Thus, anisotropy in charge transport within and out of ab-plane should be observed.

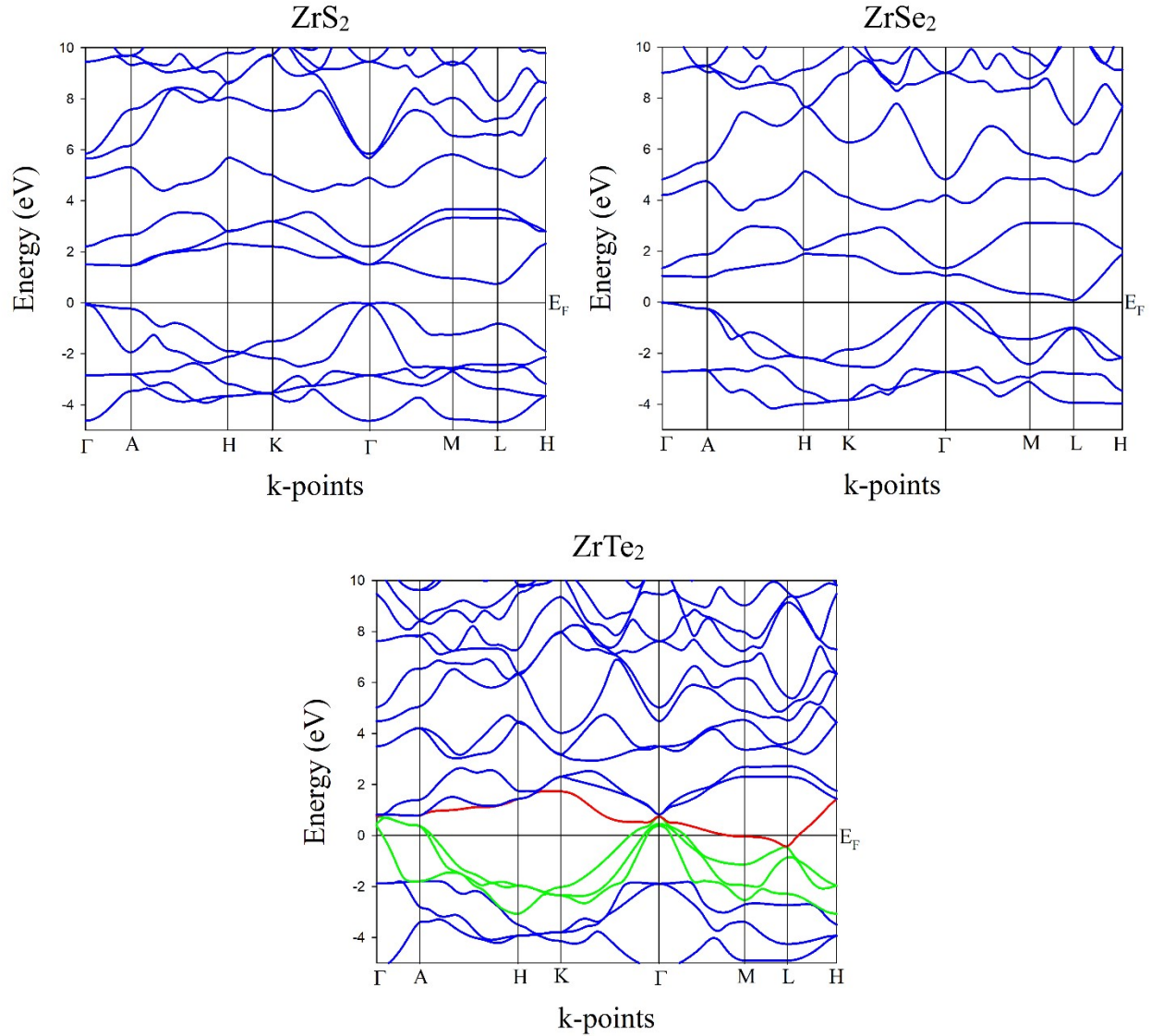


Figure 3. The band structure of ZrX_2 ($X = S, Se, Te$) compounds along the high symmetry directions of the k-space within the first Brillouin zone.

(b) Electronic energy density of states

To comprehend the electronic properties of ZrX_2 ($X = S, Se, Te$) in greater depth, the electronic energy density of states in the valence and conduction bands have been calculated using the energy dispersion curves shown in Fig. 3. Figure 4 shows the calculated total density of states (TDOS) and atom resolved partial density of states (PDOS) of ZrX_2 ($X = S, Se, Te$) compounds as a function of energy, $(E - E_F)$. The vertical dashed line at 0 eV represents the Fermi level, E_F . The TDOS of ZrS_2 and $ZrSe_2$ at Fermi level is zero, which indicates the semiconducting nature of these materials, whereas the TDOS of $ZrTe_2$ is ~ 1.0 electronic states/eV indicating its metallic

nature. This value for ZrTe_2 is in fair agreement with the previous work with a value of 0.70 electronic states/eV [83].

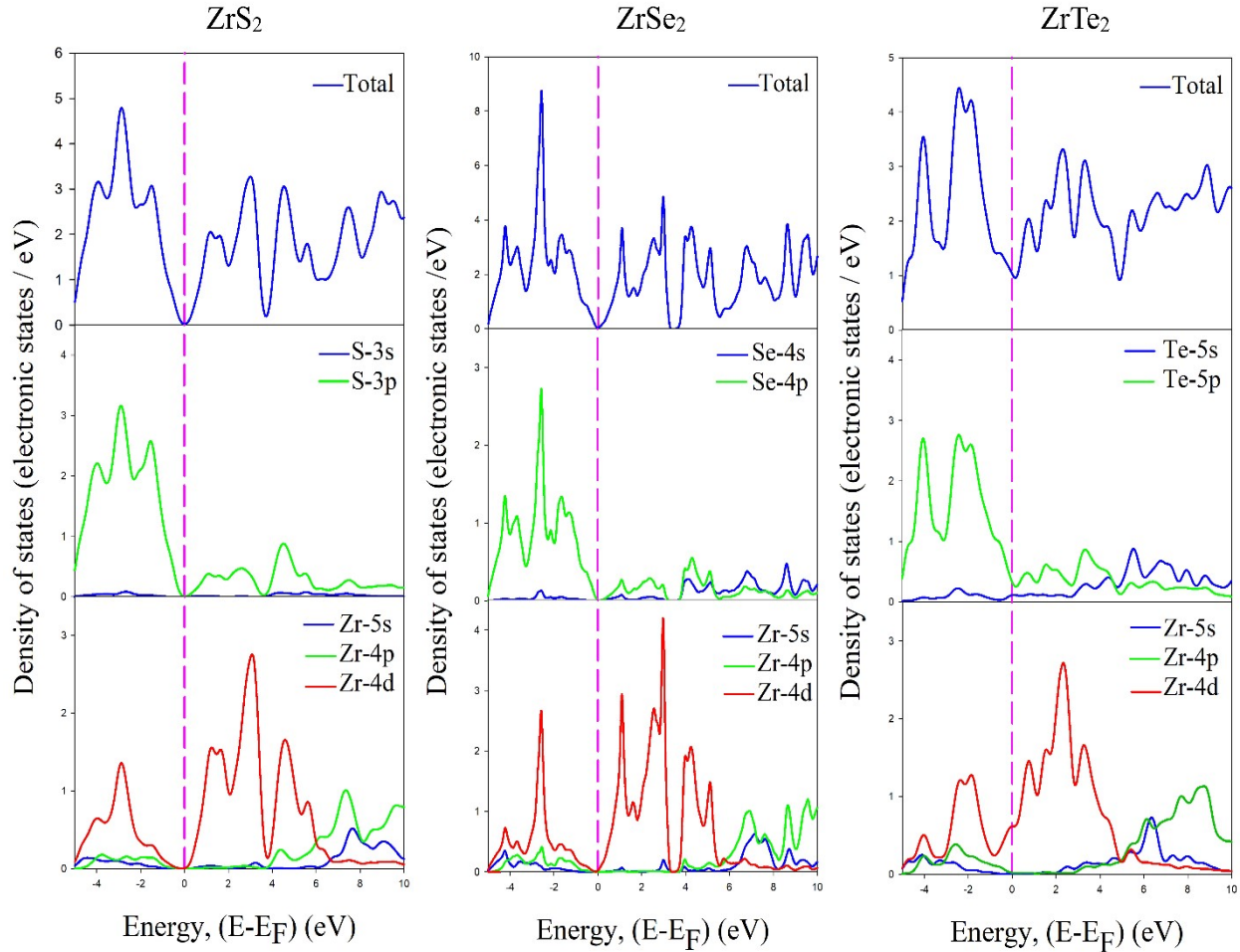


Figure 4. Total and partial density of states of ZrX_2 ($X = \text{S}, \text{Se}, \text{Te}$) compounds.

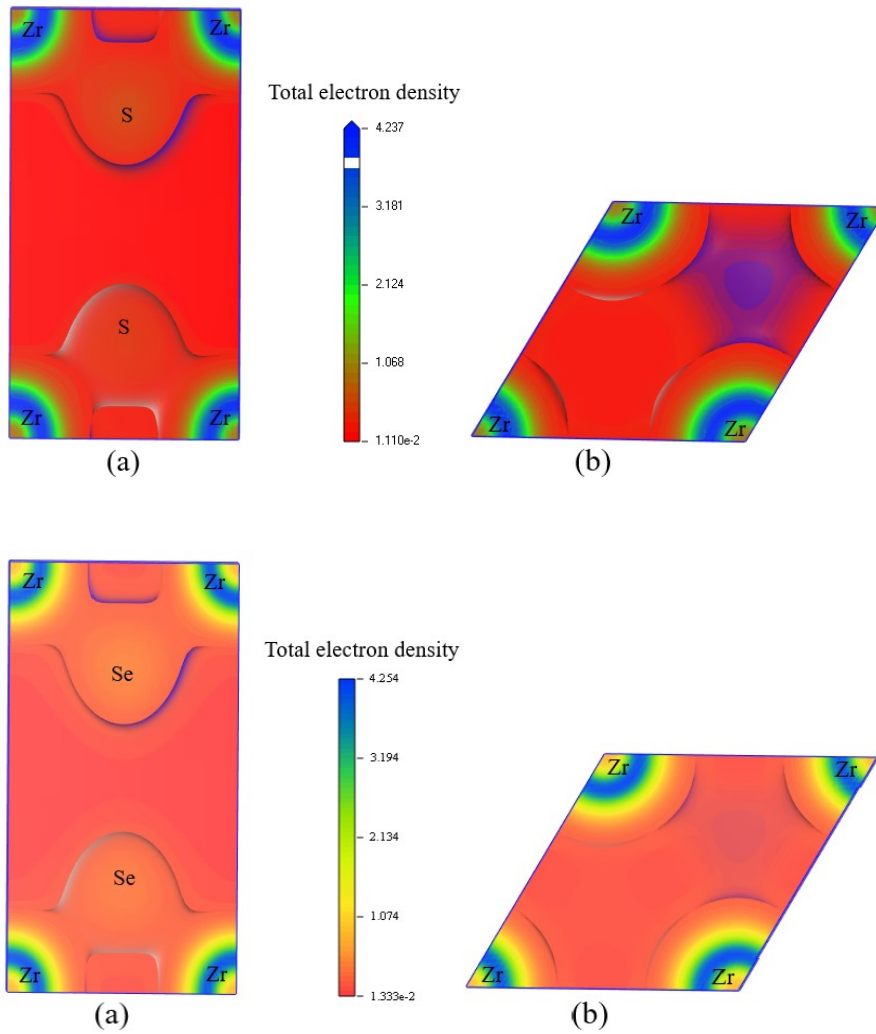
The valence bands of ZrS_2 and ZrSe_2 mainly consist of S-3p, Zr-4d electronic states and Se-4p, Zr-4d electronic states, respectively with almost equal contribution. The contributions of S-3s, Se-4s, Zr-5s, and Zr-4p orbitals to the valence band are minimal. In ZrTe_2 , the band mainly consists of Te-5p and Zr-4d electronic states having the highest contribution from Te-4p. Both these bands due to Te-5p and Zr-4d electrons cross the Fermi level and give rise to metallic behavior. On the other hand, in the conduction bands of these compounds near the Fermi level dominant contributions come from the Zr-4d electronic states. There is significant overlap in energy between the S-3p and Zr-4d bands in ZrS_2 , Se-4p and Zr-4d bands in ZrSe_2 , and Te-5p and Zr-4d bands in ZrTe_2 compounds. Such overlaps are suggestive of covalent bonding between the electronic states involved. The nearest peak at the negative energy below the Fermi level in TDOS is known as bonding peak, while the nearest peak at the positive energy is the anti-bonding peak. The energy gap between these peaks is called the pseudogap. A pseudogap very

close to E_F is an indication of high structural stability [84–87]. In ZrX_2 ($X = S, Se, Te$) compounds bonding and anti-bonding peaks are within 2 eV from Fermi level. The close proximity of the peaks in the TDOS to the Fermi energy indicates that it might be possible to change the electronic phase of these compounds by suitable atomic substitution (alloying) or by applying pressure.

IV. Charge density distribution and bonding properties

(a) Charge density distribution

To study the bonding nature between the atoms of ZrX_2 ($X = S, Se, Te$), the valence electron charge density distributions within the (100) and (001) planes are depicted in Figure 5. The color scale between the maps represents the local electron density. Red and blue colors indicate lowest and highest electron density, respectively.



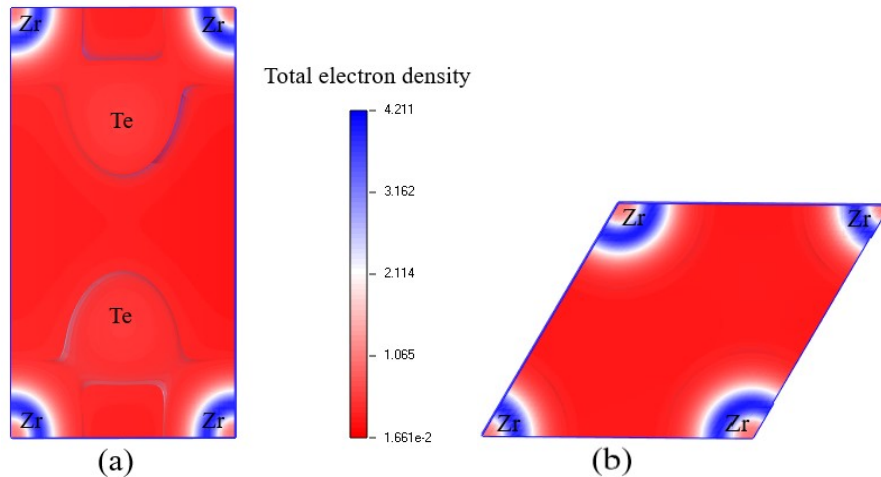


Figure 5. Charge density distribution map of ZrX_2 ($X = S, Se, Te$) in (a) (100) and (b) (001) planes.

From the above charge density distribution maps we see that the charge distribution around the X atomic species gets significantly distorted of spherical shape due to the charge distribution of the surrounding Zr atoms. This is an indication of covalent bonding. Since charge on X atoms is higher than those of the Zr atoms, there is also ionic contribution. Figs. 5b for ZrS_2 and $ZrSe_2$ show directional bonding between the Zr atoms where clear signs of charge accumulation between those are seen. This is indicative of the formation of covalent bonding between these atoms. It is interesting to note that such charge accumulation is absent for the metallic $ZrTe_2$ compound. Almost uniform charge density between the Zr atoms in $ZrTe_2$ implies that bonding between these atoms is metallic in nature. This perhaps explains why the hardness of $ZrTe_2$ is much lower than that for ZrS_2 or $ZrSe_2$.

(b) Bonding properties

We have studied both Mulliken population analysis (MPA) [88] and Hirshfeld population analysis (HPA) [89] to explore the bonding nature of ZrX_2 ($X = S, Se, Te$) compounds further. The results are disclosed in Tables 7 and 8. According to MPA, in ZrS_2 Zr atom gives up 0.29 charge to each S atom and in $ZrTe_2$ two Te atoms transfer 0.49e charge to Zr. On the other hand, no charge transfer occurs between Zr and Se atom in $ZrSe_2$. The transfer of electrons between different atoms in the compounds is due to the partial presence of ionic bonding. The difference between formal ionic charge and calculated Mulliken charge is called the effective valence charge (EVC). Non-zero EVC in all the three compounds is an indication of covalent bonding among the atoms in all these compounds (Table 7). On the other hand, according to HPA, in ZrS_2 compound Zr atom transfers 0.14e electronic charge to each S atom. This result is consistent with that of MPA. In $ZrSe_2$, Zr atom transfers 0.10e charge to each Se atom. But in $ZrTe_2$, very small amount of electronic charge is transferred to Te from Zr, which is completely opposite to MPA. Overall, the HPA results are more reliable because it is free from basis set dependence. In contrast,

Mulliken population analysis may lead to large changes of the computed atomic charges for small variations in the underlying basis sets and can overestimate the covalent character of a bond.

Table 7. Charge spilling parameter (%), orbital charges (electron), atomic Mulliken charge (electron), Hirshfeld charge (electron), and EVC (electron) of ZrX_2 ($X = S, Se, Te$).

Compound	Atoms	Charge spilling (%)	s	p	d	Total	Mulliken charge	Hirshfeld charge	EVC
ZrS ₂	S	1.13	1.85	4.44	0.0	6.27	-0.29	-0.14	1.71
	Zr		2.43	6.48	2.52	11.42	0.58	0.28	3.42
ZrSe ₂	Se	0.78	1.70	4.30	0.0	6.0	0.0	-0.10	2.0
	Zr		2.58	6.89	2.59	12.0	0.0	0.20	4.0
ZrTe ₂	Te	0.85	1.67	4.08	0.0	5.75	0.25	-0.03	1.75
	Zr		2.66	6.99	2.84	12.49	-0.49	0.07	3.51

From Table 8, it is seen that the value of overlap population are small and positive for each material. The small positive value indicates there is weak interaction between the atoms and they have bonding nature. Generally, shorter bond length represents stronger bonding and consequently higher bond strengths. Among the ZrX_2 ($X = S, Se, Te$) TMDCs, the bond lengths of Zr-S and Zr-Se are quite close. For Zr-Te, the bond lengths are higher and the bond populations are lower. This implies that the bonding strengths in $ZrTe_2$ are significantly lower. These results are completely in accord with the hardness values of ZrX_2 ($X = S, Se, Te$) obtained in the preceding section.

Table 8. Calculated bond overlap population and bond lengths (Å) for ZrX_2 ($X = S, Se, Te$) TMDCs.

Compound	Bond	Population	Length
ZrS ₂	S2 -- Zr1	1.30	2.551
	S1 -- Zr1	1.30	2.551
ZrSe ₂	Se2 -- Zr1	0.87	2.663
	Se1 -- Zr1	0.87	2.663
ZrTe ₂	Zr1 -- Te1	0.55	2.892
	Zr1 -- Te2	0.55	2.892

V. Optical properties

The understanding of energy/frequency dependent optical parameters is essential to predict how a material will respond when electromagnetic radiation is incident on it. In order to investigate possible optoelectronic applications of a compound, knowledge regarding the response of the compound to infrared, visible and ultraviolet spectra is important. Various frequency dependent optical constants, namely, dielectric function $\epsilon(\omega)$, refractive index $n(\omega)$, optical conductivity $\sigma(\omega)$, reflectivity $R(\omega)$, absorption coefficient $\alpha(\omega)$ and energy loss function $L(\omega)$ (where $\omega = 2\pi f$ is the angular frequency) are calculated in this section to explore the response of ZrX_2 ($X = S, Se, Te$) to incident photons. The optical parameters of the compounds are depicted in Figs. 6, 7 and 8 for incident energy up to 25 eV and the electric field polarizations along [100], [010], and [001] directions.

Figs. 6(a), 7(a) and 8(a) represent the absorption coefficient $\alpha(\omega)$ of ZrX_2 ($X = S, Se, Te$). The absorption coefficients start at around 0.75 eV and 0.20 eV for ZrS_2 and $ZrSe_2$ respectively, which confirms the semiconducting nature of these compounds. The onset energies also agree very well with the band gap values obtained from the band structure calculations. In $ZrTe_2$, $\sigma(\omega)$ starts from 0 eV, which is an indication of its metallic nature. All the compounds in this study exhibit a peak in the absorption spectrum in the ultraviolet region which falls down in the higher energy region for all the polarizations of the electric field. The absorption spectra suggest that these compounds can absorb ultraviolet radiation quite efficiently. The absorption spectra originate mainly from the photon induced electronic transitions between the S-3p, Se-4p, Te-5p, and Zr-4d electronic states in the valence and conduction bands for ZrS_2 , $ZrSe_2$ and $ZrTe_2$, respectively. Figures 6(b), 7(b) and 8(b) show the real and imaginary parts of optical conductivity $\sigma(\omega)$. For ZrS_2 and $ZrSe_2$ real part of $\sigma(\omega)$ start at around 0.75 eV and 0.20 eV respectively, which is another indication of their semiconducting nature. On the other hand, optical conductivity is finite at zero energy in $ZrTe_2$ indicating again its metallic character. The real and imaginary parts of dielectric constants are illustrated in Figures 6(c), 7(c) and 8(c). The real part of the dielectric constant is related to the electrical polarization of the material, while the imaginary part is linked with dielectric loss. The real part crosses zero from below at ~ 18.5 eV for ZrS_2 and $ZrSe_2$ and at ~ 20 eV for $ZrTe_2$. After that this part approaches unity. On the other hand, the imaginary part falls sharply and flattens to a low value at the same energy.

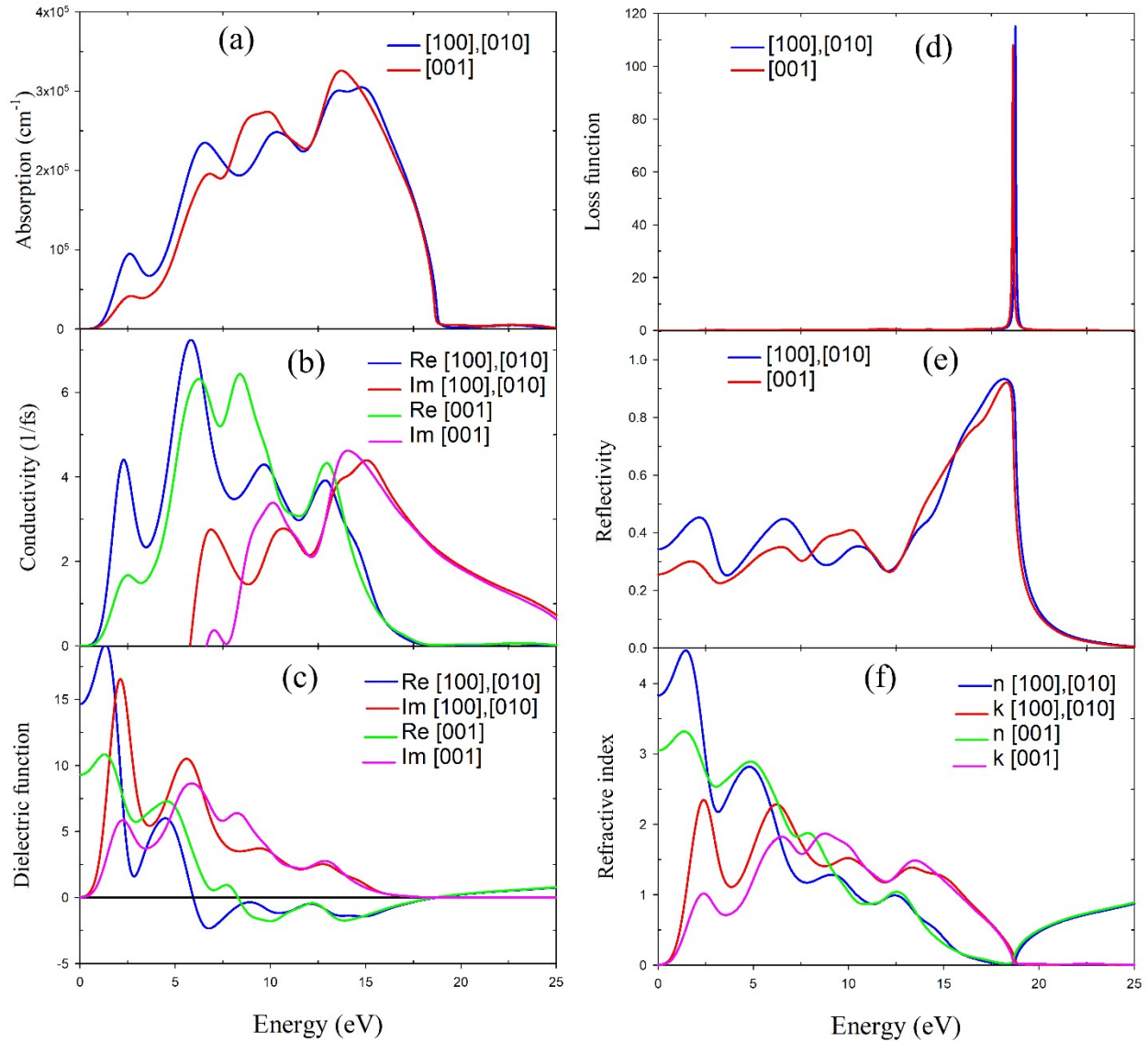


Figure 6. The frequency dependent (a) absorption coefficient (b) optical conductivity (c) dielectric function (d) loss function (e) reflectivity and (f) refractive index of ZrS_2 with electric field polarization vectors along [100], [010], and [001] directions.

The loss function $L(\omega)$ of ZrX_2 ($X = S, Se, Te$) are depicted in Figures 6(d), 7(d) and 7(d). The loss peaks are found at ~ 18.5 eV for ZrS_2 and $ZrSe_2$ and at ~ 20 eV for $ZrTe_2$. These peaks mark the characteristic plasmon energy for corresponding materials. The plasma oscillations due to collective motions of the charge carriers are induced at these particular energies. It is worth noticing that the plasma energies coincide with the sharp falls in the absorption coefficient and reflectivity. This implies that the compounds under investigation are expected to behave transparently for photons with energies greater than the plasma energy and the optical properties will show behaviors appropriate for insulating systems.

The reflectivity profile for ZrX_2 ($X = S, Se, Te$) compounds are shown in Figures 6(e), 7(e) and 8(e). The reflectivity spectra fall sharply at plasma frequency in all three compounds.

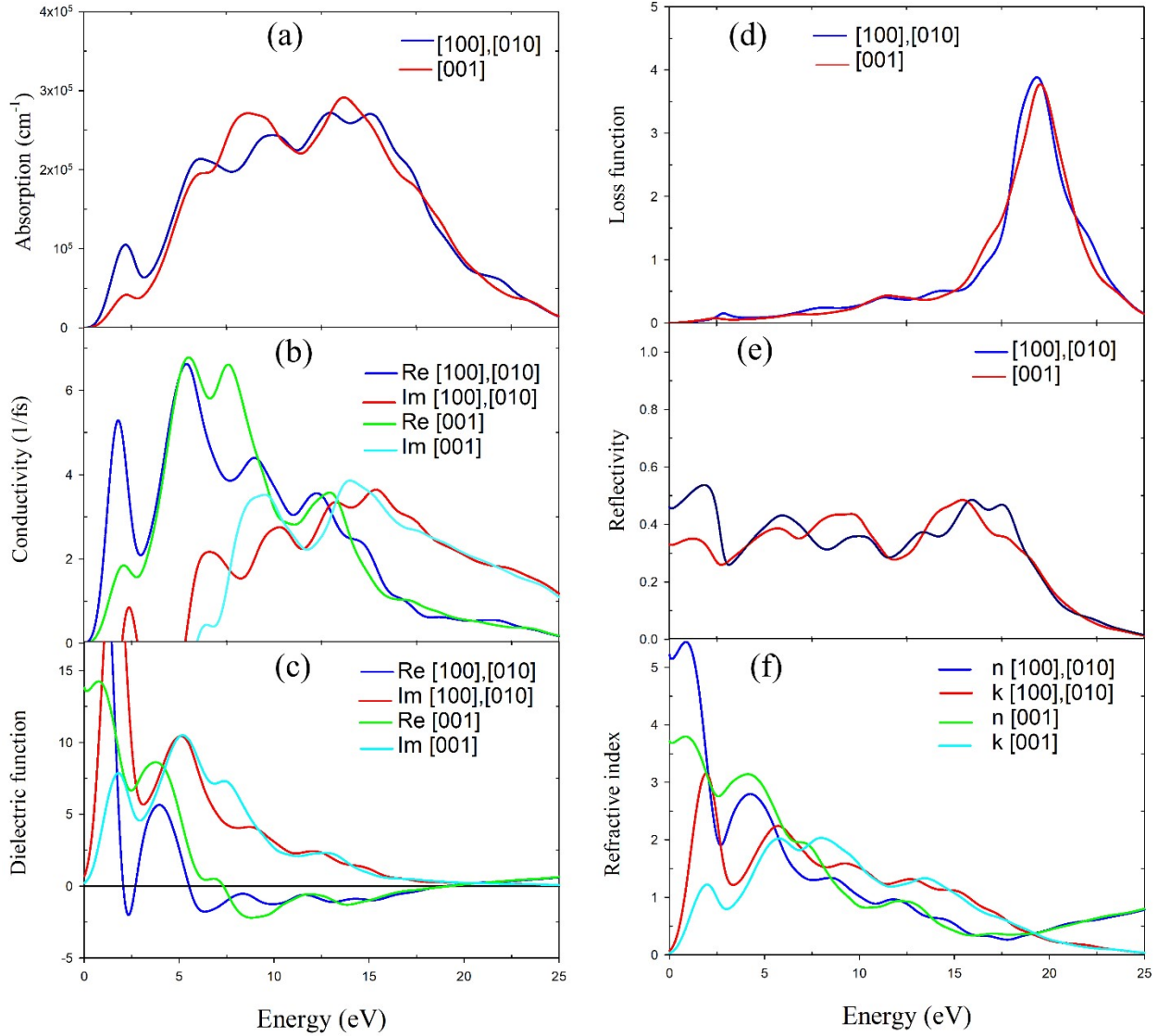


Figure 7. The frequency dependent (a) absorption coefficient (b) optical conductivity (c) dielectric function (d) loss function (e) reflectivity and (f) refractive index of $ZrSe_2$ with electric field polarization vectors along $[100]$, $[010]$, and $[001]$ directions.

Reflectivity of ZrS_2 is low in the visible and near-ultraviolet region but $R(\omega)$ rises sharply in the mid-ultraviolet energies and approaches 95% at ~ 18 eV. Therefore, this compound has the potential to be used as an efficient ultraviolet reflector in the mid-ultraviolet region. $R(\omega)$ is relatively low over a very wide energy band and displays almost non-selective character. In $ZrTe_2$, $R(\omega)$ remains over 50% in the energy range from 0 eV to ~ 20 eV. So, this material has wide band high reflectivity and can be employed as a reflector to reduce solar heating. The

frequency dependent real and imaginary parts of refractive index are represented in Figs. 6(f), 7(f) and 8(f). The phase velocity of electromagnetic wave in the material is determined by the real part of refractive index, whereas the attenuation of electromagnetic radiation inside the material is measured by the imaginary part, often referred to as extinction coefficient. The real part of refractive index has high value at low energies (0-5 eV) for both ZrS_2 and $ZrSe_2$.

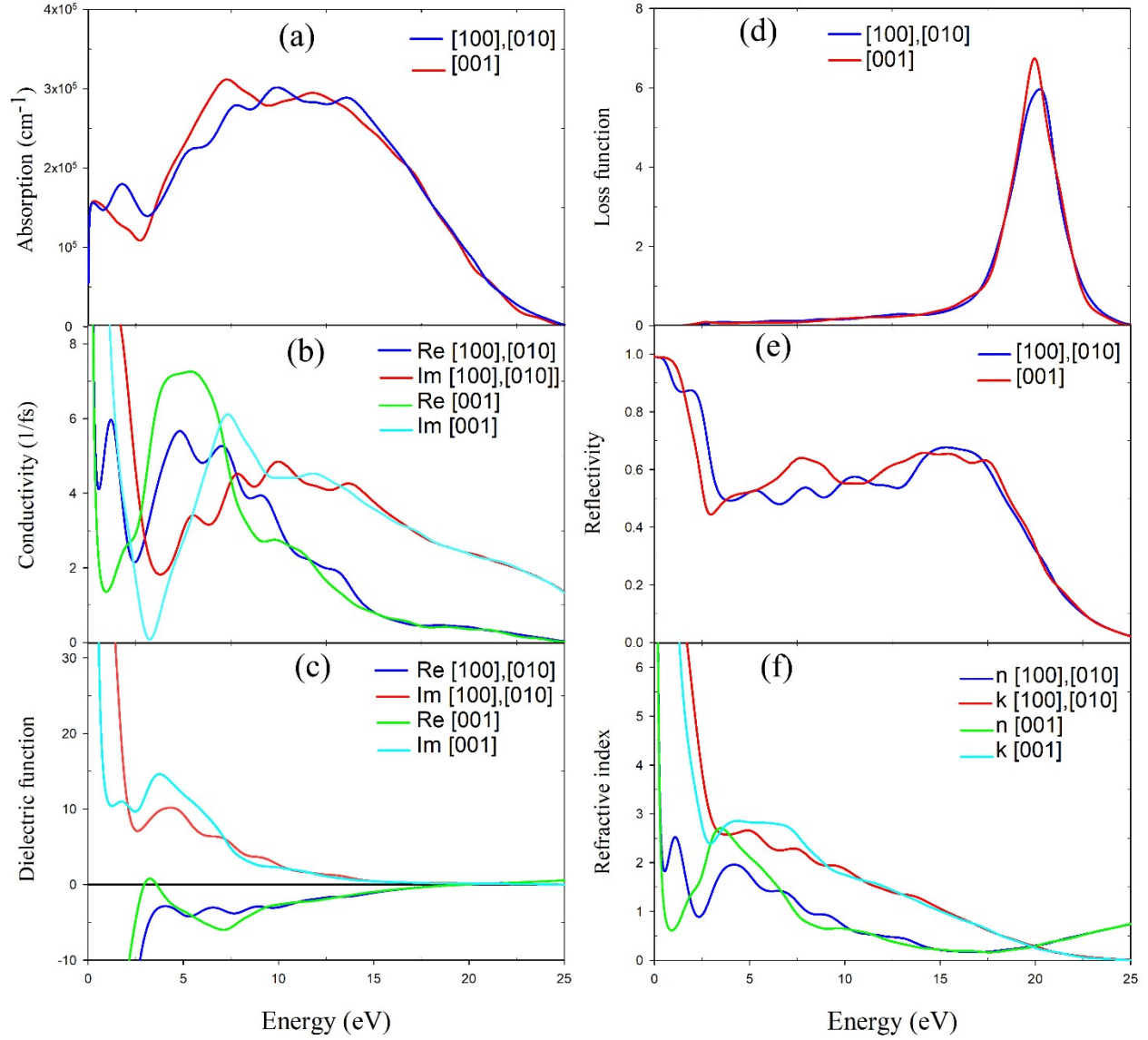


Figure 8. The frequency dependent (a) absorption coefficient (b) optical conductivity (c) dielectric function (d) loss function (e) reflectivity and (f) refractive index of $ZrTe_2$ with electric field polarization vectors along [100], [010], and [001] directions.

Therefore, the materials under study have desired optical characteristics for light emitting and optoelectronic display devices. All the optical parameters of ZrX_2 ($X = S, Se, Te$) show moderate

anisotropy with respect to the polarization direction of the electric field. Compared to other optical parameters, optical anisotropy in the refractive index is the most prominent.

VI. Thermo-physical properties

The Debye temperature, θ_D , corresponds to the highest frequency normal mode of vibration in a crystal. This temperature depends on the crystal stiffness and constituent atomic masses of the compound. θ_D is a fundamental thermo-physical parameter of solids, which is related to many physical properties such as lattice thermal conductivity, phonon specific heat, melting temperature, vacancy formation energy, bonding strength among the atoms within the crystal etc. At low temperatures only acoustic modes are responsible for vibrational excitations. Thus, at low temperature, θ_D calculated from elastic constants and specific heat are identical. In this study, θ_D is calculated from its proportionality to the mean sound velocity inside the crystal as [90],

$$\theta_D = \frac{h}{k_B} \left[\left(\frac{3n}{4\pi} \right) \frac{N_A \rho}{M} \right]^{\frac{1}{3}} v_m \quad (22)$$

where h is the Planck's constant, k_B is the Boltzmann's constant, n denotes number of atoms within the unit cell, M is molar mass, ρ is density, N_A is Avogadro's number and v_m denotes mean sound velocity. v_m can be determined from bulk (B) and shear (G) modulus through longitudinal (v_l) and transverse (v_t) sound velocities as follows,

$$v_m = \left[\frac{1}{3} \left(\frac{2}{v_t^3} + \frac{1}{v_l^3} \right) \right]^{-\frac{1}{3}} \quad (23)$$

where,

$$v_t = \sqrt{\frac{G}{\rho}} \quad (24)$$

$$v_l = \sqrt{\frac{3B + 4G}{3\rho}} \quad (25)$$

The calculated Debye temperature, θ_D with v_l , v_t and v_m are enlisted in Table 9. It is well known that, a higher Debye temperature denotes a higher phonon thermal conductivity. Fine *et al.* [91] proposed an empirical formula to determine the melting temperature of solids by using the elastic constants as follows:

$$T_m = 354 + 1.5(2C_{11} + C_{33}) \quad (26)$$

With the help of thermal conductivity the behavior of atoms inside a crystal can be understood when the crystal is heated or cooled. The hypothetical lowest value of inherent thermal conductivity is defined as the minimum thermal conductivity. This parameter is determined by the equation as follows [92–94]:

$$k_{min} = k_B v_m \left(\frac{n N_A \rho}{M} \right)^{\frac{2}{3}} (27)$$

The calculated values of T_m and k_{min} are also given in Table 9. From Table 4 and 9, it is seen that among the TMDCs under study, the Debye temperature is the largest for the compound which has highest melting temperature and highest hardness. This is expected because larger Debye temperature indicates stronger interatomic bonding that leads to higher melting temperature and elevated mechanical strength. Overall, the calculated Debye temperatures are low for all the ZrX_2 ($X = S, Se, Te$) compounds indicating the soft nature of these solids. The estimated θ_D of ZrS_2 shows very good agreement with previously obtained result [95]. Compared to many other binaries the melting temperatures of ZrX_2 ($X = S, Se, Te$) are quite low. The minimum phonon thermal conductivities are also low. Clear correspondence among θ_D , T_m , and k_{min} are observed in ZrX_2 ($X = S, Se, Te$).

Table 9. Calculated mass density (ρ in $gm\ cm^{-3}$), longitudinal, transverse and sound velocities (v_l , v_t and v_m in $km\ sec^{-1}$), and Debye temperature (θ_D in K), melting temperature (T_m in K) and minimum thermal conductivity (k_{min} in $Wm^{-1}K^{-1}$) of ZrX_2 ($X = S, Se, Te$) compounds.

Compounds	ρ	v_l	v_t	v_m	θ_D	T_m	k_{min}	Ref.
ZrS_2	3.85	3.822	2.369	2.612	276.44	779.98	0.0454	This
	-	-	-	3.996	290.87	-	-	[92]
$ZrSe_2$	5.72	3.437	2.20	2.417	249.25	750.20	0.0399	This
$ZrTe_2$	6.63	2.546	1.485	1.647	159.98	605.39	0.0241	This

4. Discussion and conclusions

Structural, elastic, electronic, bonding, optical and some thermal properties of TMDCs, ZrX_2 ($X = S, Se, Te$) compounds have been studied via ab-initio technique. Elastic anisotropy, atomic bonding character, hardness and machinability of ZrX_2 ($X = S, Se, Te$) are investigated for the first time. The band gaps of ZrS_2 and $ZrSe_2$ show systematic variation with c-axis lattice parameter and eventually vanishes (valence band overlaps with the conduction band) for $ZrTe_2$ which has a significantly larger c-axis lattice parameter compared to the other two. The change in the crystal volume closely follows the changes in atomic radii as one progressively moves from S to Te. The structural results show close agreement with previous experimental and theoretical results where available. The machinability index of ZrX_2 ($X = S, Se, Te$) are quite high, particularly so of ZrS_2 . All three TMDCs are mechanically anisotropic with mixed bonding character. Compared to ZrS_2 and $ZrSe_2$, $ZrTe_2$ is significantly softer. The optical spectra are

studied for the first time and also disclose several interesting features. All three TMDCs are good absorbers of ultraviolet radiation. Reflectivity of ZrS₂ is low in the visible and near-ultraviolet region but it increases sharply for higher photon energies and approaches 95% at ~18 eV. R(ω) spectrum of ZrTe₂, on the other hand, is non-selective and stays above 50% over a wide range of energies encompassing infrared to ultraviolet. This compound has the potential to be used as an efficient solar reflector. Furthermore, the refractive indices of ZrS₂, ZrSe₂ and ZrTe₂ in the visible range are high. Optical spectra show moderate anisotropy with respect to the polarization of the electric field of the incident light. Debye temperatures of the compounds under investigation are low, particularly of ZrTe₂. Very low θ_D of ZrTe₂ is a consequence of significantly softer lattice of this compound compared to the other two. Low values of estimated melting temperatures and minimum phonon thermal conductivity correspond very well to the calculated values of hardness and various calculated elastic moduli.

To summarize, we have presented a comprehensive study of a number of important physical properties of TMDCs ZrX₂ (X = S, Se, Te) from the point of view of their possible applications. New results should be treated as predictions and should serve as references for future studies.

Acknowledgements

S.H.N. and R.S.I. acknowledge the research grant (1151/5/52/RU/Science-07/19-20) from the Faculty of Science, University of Rajshahi, Bangladesh, which supported the computational section of this work.

Data availability

The data sets generated and/or analyzed in this study are available from the corresponding author on reasonable request.

References

- [1] Dickinson RG, Pauling L. THE CRYSTAL STRUCTURE OF MOLYBDENITE. J Am Chem Soc 1923;45:1466–71. <https://doi.org/10.1021/ja01659a020>.
- [2] Mattheiss LF. Band Structures of Transition-Metal-Dichalcogenide Layer Compounds. Phys Rev B 1973;8:3719–40. <https://doi.org/10.1103/PhysRevB.8.3719>.
- [3] Wilson JA, Yoffe AD. The transition metal dichalcogenides discussion and interpretation of the observed optical, electrical and structural properties. Adv Phys 1969;18:193–335. <https://doi.org/10.1080/00018736900101307>.
- [4] Neal AT, Du Y, Liu H, Ye PD. Two-Dimensional TaSe₂ Metallic Crystals: Spin–Orbit Scattering Length and Breakdown Current Density. ACS Nano 2014;8:9137–42. <https://doi.org/10.1021/nn5027164>.
- [5] Zhang Z, Niu J, Yang P, Gong Y, Ji Q, Shi J, et al. Van der Waals Epitaxial Growth of 2D Metallic Vanadium Diselenide Single Crystals and their Extra-High Electrical Conductivity. Adv Mater 2017;29:1702359. <https://doi.org/10.1002/adma.201702359>.
- [6] Zhang J, Yang B, Zheng H, Han X, Yan Y. Large magnetic anisotropy and strain induced enhancement of magnetic anisotropy in monolayer TaTe₂. Phys Chem Chem Phys

- 2017;19:24341–7. <https://doi.org/10.1039/C7CP04445C>.
- [7] Ali MN, Xiong J, Flynn S, Tao J, Gibson QD, Schoop LM, et al. Large, non-saturating magnetoresistance in WTe_2 . *Nature* 2014;514:205–8. <https://doi.org/10.1038/nature13763>.
- [8] Jiang J, Liu ZK, Sun Y, Yang HF, Rajamathi CR, Qi YP, et al. Signature of type-II Weyl semimetal phase in MoTe_2 . *Nat Commun* 2017;8:13973. <https://doi.org/10.1038/ncomms13973>.
- [9] Ma H, Chen P, Li B, Li J, Ai R, Zhang Z, et al. Thickness-Tunable Synthesis of Ultrathin Type-II Dirac Semimetal PtTe_2 Single Crystals and Their Thickness-Dependent Electronic Properties. *Nano Lett* 2018;18:3523–9. <https://doi.org/10.1021/acs.nanolett.8b00583>.
- [10] Thirupathaiiah S, Jha R, Pal B, Matias JS, Das PK, Sivakumar PK, et al. MoTe_2 : An uncompensated semimetal with extremely large magnetoresistance. *Phys Rev B* 2017;95:241105. <https://doi.org/10.1103/PhysRevB.95.241105>.
- [11] Zheng X, Kuriyaki H, Hirakawa K. Electrical Anisotropy of Layered Compound ZrSe_2 and HfSe_2 . *J Phys Soc Japan* 1989;58:622–6. <https://doi.org/10.1143/JPSJ.58.622>.
- [12] Lin Y-C, Dumcenco DO, Huang Y-S, Suenaga K. Atomic mechanism of the semiconducting-to-metallic phase transition in single-layered MoS_2 . *Nat Nanotechnol* 2014;9:391–6. <https://doi.org/10.1038/nnano.2014.64>.
- [13] Hill HM, Rigosi AF, Rim KT, Flynn GW, Heinz TF. Band Alignment in MoS_2/WS_2 Transition Metal Dichalcogenide Heterostructures Probed by Scanning Tunneling Microscopy and Spectroscopy. *Nano Lett* 2016;16:4831–7. <https://doi.org/10.1021/acs.nanolett.6b01007>.
- [14] Salavati M. Electronic and mechanical responses of two-dimensional HfS_2 , HfSe_2 , ZrS_2 , and ZrSe_2 from first-principles. *Front Struct Civ Eng* 2019;13:486–94. <https://doi.org/10.1007/s11709-018-0491-5>.
- [15] Porer M, Leierseder U, Ménard J-M, Dachraoui H, Mouchliadis L, Perakis IE, et al. Non-thermal separation of electronic and structural orders in a persisting charge density wave. *Nat Mater* 2014;13:857–61. <https://doi.org/10.1038/nmat4042>.
- [16] Li LJ, Zhao WJ, Liu B, Ren TH, Eda G, Loh KP. Enhancing charge-density-wave order in 1T- TiSe_2 nanosheet by encapsulation with hexagonal boron nitride. *Appl Phys Lett* 2016;109:141902. <https://doi.org/10.1063/1.4963885>.
- [17] Ma Y, Dai Y, Guo M, Niu C, Zhu Y, Huang B. Evidence of the Existence of Magnetism in Pristine VX_2 Monolayers ($X = \text{S}, \text{Se}$) and Their Strain-Induced Tunable Magnetic Properties. *ACS Nano* 2012;6:1695–701. <https://doi.org/10.1021/nm204667z>.
- [18] Zhu X, Guo Y, Cheng H, Dai J, An X, Zhao J, et al. Signature of coexistence of superconductivity and ferromagnetism in two-dimensional NbSe_2 triggered by surface molecular adsorption. *Nat Commun* 2016;7:11210. <https://doi.org/10.1038/ncomms11210>.
- [19] Xiang H, Xu B, Xia Y, Yin J, Liu Z. Strain tunable magnetism in SnX_2 ($X = \text{S}, \text{Se}$) monolayers by hole doping. *Sci Rep* 2016;6:39218. <https://doi.org/10.1038/srep39218>.
- [20] Joe YI, Chen XM, Ghaemi P, Finkelstein KD, de la Peña GA, Gan Y, et al. Emergence of charge density wave domain walls above the superconducting dome in 1T- TiSe_2 . *Nat Phys* 2014;10:421–5. <https://doi.org/10.1038/nphys2935>.
- [21] Liu C-X. Unconventional Superconductivity in Bilayer Transition Metal Dichalcogenides. *Phys Rev Lett* 2017;118:087001. <https://doi.org/10.1103/PhysRevLett.118.087001>.
- [22] de la Barrera SC, Sinko MR, Gopalan DP, Sivadas N, Seyler KL, Watanabe K, et al. Tuning Ising superconductivity with layer and spin-orbit coupling in two-dimensional transition-metal dichalcogenides. *Nat Commun* 2018;9:1427.

- <https://doi.org/10.1038/s41467-018-03888-4>.
- [23] Mak KF, Lee C, Hone J, Shan J, Heinz TF. Atomically Thin MoS₂: A New Direct-Gap Semiconductor. *Phys Rev Lett* 2010;105:136805. <https://doi.org/10.1103/PhysRevLett.105.136805>.
- [24] Kumar A, Ahluwalia PK. Electronic structure of transition metal dichalcogenides monolayers 1H-MX₂ (M = Mo, W; X = S, Se, Te) from ab-initio theory: new direct band gap semiconductors. *Eur Phys J B* 2012;85:186. <https://doi.org/10.1140/epjb/e2012-30070-x>.
- [25] Choi W, Choudhary N, Han GH, Park J, Akinwande D, Lee YH. Recent development of two-dimensional transition metal dichalcogenides and their applications. *Mater Today* 2017;20:116–30. <https://doi.org/10.1016/j.mattod.2016.10.002>.
- [26] Späh R, Elrod U, Lux-Steiner M, Bucher E, Wagner S. p n junctions in tungsten diselenide. *Appl Phys Lett* 1983;43:79–81. <https://doi.org/10.1063/1.94128>.
- [27] Jiménez D. Drift-diffusion model for single layer transition metal dichalcogenide field-effect transistors. *Appl Phys Lett* 2012;101:243501. <https://doi.org/10.1063/1.4770313>.
- [28] Wang QH, Kalantar-Zadeh K, Kis A, Coleman JN, Strano MS. Electronics and optoelectronics of two-dimensional transition metal dichalcogenides. *Nat Nanotechnol* 2012;7:699–712. <https://doi.org/10.1038/nnano.2012.193>.
- [29] Zeng H, Dai J, Yao W, Xiao D, Cui X. Valley polarization in MoS₂ monolayers by optical pumping. *Nat Nanotechnol* 2012;7:490–3. <https://doi.org/10.1038/nnano.2012.95>.
- [30] Cheng R, Jiang S, Chen Y, Liu Y, Weiss N, Cheng H-C, et al. Few-layer molybdenum disulfide transistors and circuits for high-speed flexible electronics. *Nat Commun* 2014;5:5143. <https://doi.org/10.1038/ncomms6143>.
- [31] Li SJ, Bernède JC, Pouzet J, Jamali M. thin films prepared by solid state reaction (induced by annealing) between the constituents in thin film form. *J Phys Condens Matter* 1996;8:2291–304. <https://doi.org/10.1088/0953-8984/8/14/006>.
- [32] Fuhrer MS, Hone J. Measurement of mobility in dual-gated MoS₂ transistors. *Nat Nanotechnol* 2013;8:146–7. <https://doi.org/10.1038/nnano.2013.30>.
- [33] Wu W, Wang L, Li Y, Zhang F, Lin L, Niu S, et al. Piezoelectricity of single-atomic-layer MoS₂ for energy conversion and piezotronics. *Nature* 2014;514:470–4. <https://doi.org/10.1038/nature13792>.
- [34] Gong C, Zhang Y, Chen W, Chu J, Lei T, Pu J, et al. Electronic and Optoelectronic Applications Based on 2D Novel Anisotropic Transition Metal Dichalcogenides. *Adv Sci* 2017;4:1700231. <https://doi.org/10.1002/advs.201700231>.
- [35] Khan MA, Leuenberger MN. Optoelectronics with single layer group-VIB transition metal dichalcogenides. *Nanophotonics* 2018;7:1589–600. <https://doi.org/10.1515/nanoph-2018-0041>.
- [36] Kar I, Chatterjee J, Harnagea L, Kushnirenko Y, Fedorov A V., Shrivastava D, et al. Metal-chalcogen bond-length induced electronic phase transition from semiconductor to topological semimetal in ZrX₂ (X=Se and Te). *Phys Rev B* 2020;101:165122. <https://doi.org/10.1103/PhysRevB.101.165122>.
- [37] Burkov AA. Topological semimetals. *Nat Mater* 2016;15:1145–8. <https://doi.org/10.1038/nmat4788>.
- [38] Bao W, Cai X, Kim D, Sridhara K, Fuhrer MS. High mobility ambipolar MoS₂ field-effect transistors: Substrate and dielectric effects. *Appl Phys Lett* 2013;102:042104. <https://doi.org/10.1063/1.4789365>.

- [39] Frey GL, Elani S, Homyonfer M, Feldman Y, Tenne R. Optical-absorption spectra of inorganic fullerenelike MS_2 ($M=Mo, W$). *Phys Rev B* 1998;57:6666–71. <https://doi.org/10.1103/PhysRevB.57.6666>.
- [40] Islam MR, Kang N, Bhanu U, Paudel HP, Erementchouk M, Tetard L, et al. Tuning the electrical property via defect engineering of single layer MoS_2 by oxygen plasma. *Nanoscale* 2014;6:10033. <https://doi.org/10.1039/C4NR02142H>.
- [41] Choudhary N, Islam MR, Kang N, Tetard L, Jung Y, Khondaker SI. Two-dimensional lateral heterojunction through bandgap engineering of MoS_2 via oxygen plasma. *J Phys Condens Matter* 2016;28:364002. <https://doi.org/10.1088/0953-8984/28/36/364002>.
- [42] Pumera M, Sofer Z, Ambrosi A. Layered transition metal dichalcogenides for electrochemical energy generation and storage. *J Mater Chem A* 2014;2:8981–7. <https://doi.org/10.1039/C4TA00652F>.
- [43] Vogel EM, Robinson JA. Two-dimensional layered transition-metal dichalcogenides for versatile properties and applications. *MRS Bull* 2015;40:558–63. <https://doi.org/10.1557/mrs.2015.120>.
- [44] Bastos CMO, Besse R, Da Silva JLF, Sipahi GM. Ab initio investigation of structural stability and exfoliation energies in transition metal dichalcogenides based on Ti-, V-, and Mo-group elements. *Phys Rev Mater* 2019;3:044002. <https://doi.org/10.1103/PhysRevMaterials.3.044002>.
- [45] Zhao Q, Guo Y, Si K, Ren Z, Bai J, Xu X. Elastic, electronic, and dielectric properties of bulk and monolayer ZrS_2 , $ZrSe_2$, HfS_2 , $HfSe_2$ from van der Waals density-functional theory. *Phys Status Solidi* 2017;254:1700033. <https://doi.org/10.1002/pssb.201700033>.
- [46] Jiang H. Structural and electronic properties of ZrX_2 and HfX_2 ($X = S$ and Se) from first principles calculations. *J Chem Phys* 2011;134:204705. <https://doi.org/10.1063/1.3594205>.
- [47] Tributsch H. Photo-intercalation: Possible application in solar energy devices. *Appl Phys* 1980;23:61–71. <https://doi.org/10.1007/BF00899572>.
- [48] Kohn W, Sham LJ. Self-Consistent Equations Including Exchange and Correlation Effects. *Phys Rev* 1965;140:A1133–8. <https://doi.org/10.1103/PhysRev.140.A1133>.
- [49] Clark SJ, Segall MD, Pickard CJ, Hasnip PJ, Probert MIJ, Refson K, et al. First principles methods using CASTEP. *Zeitschrift Für Krist - Cryst Mater* 2005;220:567–70. <https://doi.org/10.1524/zkri.220.5.567.65075>.
- [50] Perdew JP, Burke K, Ernzerhof M. Generalized Gradient Approximation Made Simple. *Phys Rev Lett* 1996;77:3865–8. <https://doi.org/10.1103/PhysRevLett.77.3865>.
- [51] Perdew JP, Ruzsinszky A, Csonka GI, Vydrov OA, Scuseria GE, Constantin LA, et al. Restoring the Density-Gradient Expansion for Exchange in Solids and Surfaces. *Phys Rev Lett* 2008;100:136406. <https://doi.org/10.1103/PhysRevLett.100.136406>.
- [52] Barua P, Hossain MM, Ali MA, Uddin MM, Naqib SH, Islam AKMA. Effects of transition metals on physical properties of M_2BC ($M = V, Nb, Mo$ and Ta): A DFT calculation. *J Alloys Compd* 2019;770:523–34. <https://doi.org/10.1016/j.jallcom.2018.08.155>.
- [53] Hu K, Wu M, Hinokuma S, Ohto T, Wakisaka M, Fujita JI, et al. Boosting electrochemical water splitting: via ternary NiMoCo hybrid nanowire arrays. *J Mater Chem A* 2019;7:2156–64. <https://doi.org/10.1039/c8ta11250a>.
- [54] Fischer TH, Almlof J. General methods for geometry and wave function optimization. *J Phys Chem* 1992;96:9768–74. <https://doi.org/10.1021/j100203a036>.

- [55] Naher MI, Parvin F, Islam AKMA, Naqib SH. Physical properties of niobium-based intermetallics (Nb_3B ; $B = Os, Pt, Au$): a DFT-based ab-initio study. *Eur Phys J B* 2018;91:289. <https://doi.org/10.1140/epjb/e2018-90388-9>.
- [56] Nasir MT, Hadi MA, Rayhan MA, Ali MA, Hossain MM, Roknuzzaman M, et al. First-Principles Study of Superconducting ScRhP and ScIrP pnictides. *Phys Status Solidi Basic Res* 2017;254:1–10. <https://doi.org/10.1002/pssb.201700336>.
- [57] Hadi MA, Alam MA, Roknuzzaman M, Nasir MT, Islam AKMA, Naqib SH. Structural, elastic, and electronic properties of recently discovered ternary silicide superconductor Li_2IrSi_3 : An ab-initio study. *Chinese Phys B* 2015;24:117401. <https://doi.org/10.1088/1674-1056/24/11/117401>.
- [58] Friend RH, Yoffe AD. Electronic properties of intercalation complexes of the transition metal dichalcogenides. *Adv Phys* 1987;36:1–94. <https://doi.org/10.1080/00018738700101951>.
- [59] Greenaway DL, Nitsche R. Preparation and optical properties of group IV–VI₂ chalcogenides having the CdI_2 structure. *J Phys Chem Solids* 1965;26:1445–58. [https://doi.org/10.1016/0022-3697\(65\)90043-0](https://doi.org/10.1016/0022-3697(65)90043-0).
- [60] Mouhat F, Coudert F-X. Necessary and sufficient elastic stability conditions in various crystal systems. *Phys Rev B* 2014;90:224104. <https://doi.org/10.1103/PhysRevB.90.224104>.
- [61] Voigt W. *Lehrbuch der kristallphysik (mit ausschluß der kristalloptik)*. Leipzig; Berlin; [Ann Arbor, Mich.]: B.G. Teubner [J.W. Edwards]; 1946.
- [62] Reuss A. Berechnung der Fließgrenze von Mischkristallen auf Grund der Plastizitätsbedingung für Einkristalle . *ZAMM - Zeitschrift Für Angew Math Und Mech* 1929;9:49–58. <https://doi.org/10.1002/zamm.19290090104>.
- [63] Hill R. The Elastic Behaviour of a Crystalline Aggregate. *Proc Phys Soc Sect A* 1952;65:349–54. <https://doi.org/10.1088/0370-1298/65/5/307>.
- [64] Pugh SF. XCII. Relations between the elastic moduli and the plastic properties of polycrystalline pure metals. *London, Edinburgh, Dublin Philos Mag J Sci* 1954;45:823–43. <https://doi.org/10.1080/14786440808520496>.
- [65] Greaves GN, Greer AL, Lakes RS, Rouxel T. Poisson's ratio and modern materials. *Nat Mater* 2011;10:823–37. <https://doi.org/10.1038/nmat3134>.
- [66] Anderson OL, Demarest HH. Elastic constants of the central force model for cubic structures: Polycrystalline aggregates and instabilities. *J Geophys Res* 1971;76:1349–69. <https://doi.org/10.1029/JB076i005p01349>.
- [67] Kleinman L. Deformation Potentials in Silicon. I. Uniaxial Strain. *Phys Rev* 1962;128:2614–21. <https://doi.org/10.1103/PhysRev.128.2614>.
- [68] Sun Z, Music D, Ahuja R, Schneider JM. Theoretical investigation of the bonding and elastic properties of nanolayered ternary nitrides. *Phys Rev B* 2005;71:193402. <https://doi.org/10.1103/PhysRevB.71.193402>.
- [69] Hadi MA, Christopoulos S-RG, Naqib SH, Chronos A, Fitzpatrick ME, Islam AKMA. Physical properties and defect processes of M_3SnC_2 ($M = Ti, Zr, Hf$) MAX phases: Effect of M-elements. *J Alloys Compd* 2018;748:804–13. <https://doi.org/10.1016/j.jallcom.2018.03.182>.
- [70] Roknuzzaman M, Hadi MA, Abden MJ, Nasir MT, Islam AKMA, Ali MS, et al. Physical properties of predicted Ti_2CdN versus existing Ti_2CdC MAX phase: An ab initio study. *Comput Mater Sci* 2016;113:148–53. <https://doi.org/10.1016/j.commatsci.2015.11.039>.

- [71] Chowdhury A, Ali MA, Hossain MM, Uddin MM, Naqib SH, Islam AKMA. Predicted MAX Phase Sc_2InC : Dynamical Stability, Vibrational and Optical Properties. *Phys Status Solidi* 2018;255:1700235. <https://doi.org/10.1002/pssb.201700235>.
- [72] Ali MA, Hossain MM, Uddin MM, Hossain MA, Islam AKMA, Naqib SH. Physical properties of new MAX phase borides M_2SB ($\text{M} = \text{Zr}, \text{Hf}$ and Nb) in comparison with conventional MAX phase carbides M_2SC ($\text{M} = \text{Zr}, \text{Hf}$ and Nb): Comprehensive insights. *J Mater Res Technol* 2021;11:1000–18. <https://doi.org/10.1016/j.jmrt.2021.01.068>.
- [73] Ali MA, Hossain MM, Uddin MM, Islam AKMA, Jana D, Naqib SH. DFT insights into new B-containing 212 MAX phases: Hf_2AB_2 ($\text{A} = \text{In}, \text{Sn}$). *J Alloys Compd* 2021;860:158408. <https://doi.org/10.1016/j.jallcom.2020.158408>.
- [74] Afzal MA, Naqib SH. A DFT based first-principles investigation of optoelectronic and structural properties of $\text{Bi}_2\text{Te}_2\text{Se}$. *Phys Scr* 2021;96:045810. <https://doi.org/10.1088/1402-4896/abe2d2>.
- [75] Rahman Rano B, Syed IM, Naqib SH. Elastic, electronic, bonding, and optical properties of WTe_2 Weyl semimetal: A comparative investigation with MoTe_2 from first principles. *Results Phys* 2020;19:103639. <https://doi.org/10.1016/j.rinp.2020.103639>.
- [76] Mridha MM, Naqib SH. Pressure dependent elastic, electronic, superconducting, and optical properties of ternary barium phosphides (BaM_2P_2 ; $\text{M} = \text{Ni}, \text{Rh}$): DFT based insights. *Phys Scr* 2020;95:105809. <https://doi.org/10.1088/1402-4896/abb968>.
- [77] Kube CM. Elastic anisotropy of crystals. *AIP Adv* 2016;6:095209. <https://doi.org/10.1063/1.4962996>.
- [78] Ravindran P, Fast L, Korzhavyi PA, Johansson B, Wills J, Eriksson O. Density functional theory for calculation of elastic properties of orthorhombic crystals: Application to TiSi_2 . *J Appl Phys* 1998;84:4891–904. <https://doi.org/10.1063/1.368733>.
- [79] Ranganathan SI, Ostoja-Starzewski M. Universal Elastic Anisotropy Index. *Phys Rev Lett* 2008;101:055504. <https://doi.org/10.1103/PhysRevLett.101.055504>.
- [80] Kube CM, de Jong M. Elastic constants of polycrystals with generally anisotropic crystals. *J Appl Phys* 2016;120:165105. <https://doi.org/10.1063/1.4965867>.
- [81] Gaillac R, Pullumbi P, Coudert F-X. ELATE: an open-source online application for analysis and visualization of elastic tensors. *J Phys Condens Matter* 2016;28:275201. <https://doi.org/10.1088/0953-8984/28/27/275201>.
- [82] Moustafa M, Zandt T, Janowitz C, Manzke R. Growth and band gap determination of the $\text{ZrS}_x\text{Se}_{2-x}$ single crystal series. *Phys Rev B* 2009;80:035206. <https://doi.org/10.1103/PhysRevB.80.035206>.
- [83] Aryasetiawan F, Gunnarsson O. The GW method. *Reports Prog Phys* 1998;61:237–312. <https://doi.org/10.1088/0034-4885/61/3/002>.
- [84] Reshak AH, Auluck S. Theoretical investigation of the electronic and optical properties of ZrX_2 ($\text{X} = \text{S}, \text{Se}$ and Te). *Phys B Condens Matter* 2004;353:230–7. <https://doi.org/10.1016/j.physb.2004.10.001>.
- [85] Parvin F, Naqib SH. Pressure dependence of structural, elastic, electronic, thermodynamic, and optical properties of van der Waals-type NaSn_2P_2 pnictide superconductor: Insights from DFT study. *Results Phys* 2021;21:103848. <https://doi.org/10.1016/j.rinp.2021.103848>.
- [86] Naher MI, Naqib SH. Structural, elastic, electronic, bonding, and optical properties of topological CaSn_3 semimetal. *J Alloys Compd* 2020;829:154509. <https://doi.org/10.1016/j.jallcom.2020.154509>.

- [87] Xu J-H, Oguchi T, Freeman AJ. Crystal structure, phase stability, and magnetism in Ni_3V . *Phys Rev B* 1987;35:6940–3. <https://doi.org/10.1103/PhysRevB.35.6940>.
- [88] Mulliken RS. Electronic Population Analysis on LCAO–MO Molecular Wave Functions. I. *J Chem Phys* 1955;23:1833–40. <https://doi.org/10.1063/1.1740588>.
- [89] Hirshfeld FL. Bonded-atom fragments for describing molecular charge densities. *Theor Chim Acta* 1977;44:129–38. <https://doi.org/10.1007/BF00549096>.
- [90] Anderson OL. A simplified method for calculating the debye temperature from elastic constants. *J Phys Chem Solids* 1963;24:909–17. [https://doi.org/10.1016/0022-3697\(63\)90067-2](https://doi.org/10.1016/0022-3697(63)90067-2).
- [91] Fine M, Brown L, Marcus H. Elastic constants versus melting temperature in metals. *Scr Metall* 1984;18:951–6. [https://doi.org/10.1016/0036-9748\(84\)90267-9](https://doi.org/10.1016/0036-9748(84)90267-9).
- [92] Clarke DR. Materials selection guidelines for low thermal conductivity thermal barrier coatings. *Surf Coatings Technol* 2003;163–164:67–74. [https://doi.org/10.1016/S0257-8972\(02\)00593-5](https://doi.org/10.1016/S0257-8972(02)00593-5).
- [93] Hossain MM, Ali MA, Uddin MM, Hossain MA, Rasadujjaman M, Naqib SH, et al. Influence of Se doping on recently synthesized $\text{NaInS}_{2-x}\text{Se}_x$ solid solutions for potential thermo-mechanical applications studied via first-principles method. *Mater Today Commun* 2021;26:101988. <https://doi.org/10.1016/j.mtcomm.2020.101988>.
- [94] Hossain MM, Hossain MA, Moon SA, Ali MA, Uddin MM, Naqib SH, et al. NaInX_2 (X = S, Se) layered materials for energy harvesting applications: first-principles insights into optoelectronic and thermoelectric properties. *J Mater Sci Mater Electron* 2021. <https://doi.org/10.1007/s10854-020-05131-7>.
- [95] Pike NA, Dewandre A, Van Troeye B, Gonze X, Verstraete MJ. Vibrational and dielectric properties of the bulk transition metal dichalcogenides. *Phys Rev Mater* 2018;2:063608. <https://doi.org/10.1103/PhysRevMaterials.2.063608>.

Author Contributions

M.M. and M.A.A. performed the theoretical calculations and contributed to the analysis. R.S.I. contributed to the writing of the manuscript. S.H.N. designed the project, analyzed the results, and finalized the manuscript. All the authors reviewed the manuscript.

Additional Information

Competing Interests

The authors declare no competing interests.